International Journal of Impact Engineering 53 (2013) 29–43

Contents lists available at SciVerse ScienceDirect

International Journal of Impact Engineering

journal homepage: www.elsevier.com/locate/ijimpeng

Dynamic crushing of cellular materials: A unified framework of plastic shock wave models

Zhijun Zheng*, Jilin Yu, Changfeng Wang, Shenfei Liao, Yaodong Liu

CAS Key Laboratory of Mechanical Behavior and Design of Materials, University of Science and Technology of China, Hefei, Anhui 230026, PR China

ARTICLE INFO

Article history:
Received 14 November 2011
Received in revised form
18 March 2012
Accepted 10 June 2012
Available online 26 September 2012

Keywords:
Cellular material
Deformation localisation
Shock front
Strength enhancement
Voronoi structure

ABSTRACT

Strength enhancement and deformation localisation are typical features of the dynamic response of cellular materials. Several one-dimensional shock models have been developed to explain these features. A unified framework of one-dimensional plastic shock wave models was established in this paper. Based on an arbitrary plastic hardening constitutive model for cellular materials, general solutions, although implicit, have been derived for two impact scenarios. For a rigid–power-law hardening (R-PLH) idealisation involved in three material parameters, namely the yield stress, the strength index and the strain-hardening index, closed-form/semi-closed-form solutions of the physical quantities across the shock front have been derived. The linearly hardening and locking idealisations are found to correspond to the two opposite limit cases with the strain-hardening index of one and infinity, respectively. The shock models based on three different idealisations are verified with cell-based finite element models including an irregular honeycomb and a closed-cell foam. It is found that the force responses predicted by the shock models are not very sensitive to the choice of the idealisations and they are in good agreement with the cell-based finite element results. Deformation features predicted by the shock models are compared well with the cell-based results when the impact velocity is not very low. The comparisons show that using more realistic constitutive models such as the R-PLH idealisation may present more accurate predictions.

1. Introduction

Cellular materials such as metallic foams and honeycombs have been extensively used as impact energy absorbers and blast protectors. Strength enhancement and deformation localisation are typical features of their dynamic responses. These features are mainly caused by inertia and well explained by several crushing models, especially the continuum-based shock models as reviewed below.

A simple one-dimensional shock model was first proposed by Reid and Peng [1] to explain the strength enhancement of wood specimens subjected to impact against a rigid target. For simplicity, they modelled the wood using a rate-independent, rigid–perfectly plastic–locking (R-P-P-L) idealisation including two key parameters, i.e. the plateau stress σ_{pl} and the locking strain ε_L. The later parameter is usually assumed to equal the densification strain ε_D. By analysing the stress discontinuity across the shock front, an elegant solution for the stress behind the shock front has been presented as [1–4]

$$\sigma_B = \sigma_{pl} + \rho_0 v^2/\varepsilon_L, \tag{1}$$

where ρ_0 is the initial density of the cellular material and v the particle velocity behind the shock front. A numerical scheme, e.g. a fourth-order Runge-Kutta numerical scheme [4], should be used to determine the velocity v when considering its temporal change. Based on this simple model, a first order understanding has been produced for the dynamic crushing strength enhancement of cellular materials, such as wood [1], aluminium honeycombs [2] and aluminium foams [3,4]. The R-P-P-L idealisation was also used to model the crushing of a foam with blast loading [5,6], with mass loading [4] or impacting a free mass [7].

The deformation patterns of cellular materials under compression are very complex, but they can be catalogued into three deformation modes according to the deformation mechanisms under different impact velocities, namely the Homogeneous Mode, the Transitional Mode and the Shock Mode [8,9]. A rigid–linear hardening plastic–locking (R-LHP-L) idealisation was employed by

* Corresponding author. Tel.: +86 551 360 3044; fax: +86 551 360 6459.
E-mail address: zjzheng@ustc.edu.cn (Z. Zheng).

0734-743X/$ – see front matter © 2012 Elsevier Ltd. All rights reserved.
http://dx.doi.org/10.1016/j.ijimpeng.2012.06.012

Zheng et al. [10] to develop a Shock-Mode model for high-velocity impact and a Transitional-Mode model for moderate-velocity impact. This idealisation has three parameters including the yield stress σ_0, the plastic hardening modulus E_1 and the locking strain ε_L. Two impact scenarios considered in the literature [1,4] have been revisited: the *rod-target impact* (a cellular material rod with a backing mass striking axially against a stationary target) and the *striker-rod impact* (a rigid striker striking axially against a stationary cellular material rod with a fixed wall at the distal end). Some closed-form solutions such as those for the striker-rod impact scenario (see Eqs. (53) and (54) in the present paper) have been derived.

The elastic property may strongly affect the response of cellular materials under low-velocity impact. An elastic-perfectly plastic–rigid (E-P-P-R) idealisation and an elastic–plastic–rigid (E-P-R) idealisation have been employed by Lopatnikov et al. [11–13] to consider the elastic effect. They used the E-P-P-R idealisation, which has three key parameters (the elastic modulus E_0, the plateau stress σ_{pl} and the maximum possible strain ε_{max}), to investigate both Taylor impact and plate impact of aluminium foams [11,12]. Four significantly different possibilities of impact velocity were suggested by Lopatnikov et al. [12] and improved by Li and Reid [14]. The E-P-R idealisation was used to derive the energy absorbed under quasi-static compression of cellular materials when the wave propagation effects were neglected [13].

All the above idealisations mentioned have a locking stage, but different locking strains have been suggested. In fact, predictions are very sensitive to the locking strain [15,16]. The dynamic densification strain increases with the increase of impact velocity as found in regular honeycombs [17] and its limit is much higher than the quasi-static one, which was used as the locking strain in most papers mentioned above. Several idealisations with a nonlinear plastic hardening stage have been proposed to improve the prediction precision of shock models [16,18,19]. A rigid–softening–hardening (R-S-H) idealisation and an elastic–softening–hardening (E-S-H) idealisation have been used by Harrigan et al. [18] to model the rod-target impact and the striker-rod impact of wood along the grain. Harrigan et al. [19] also used an elastic-perfectly plastic hardening (E-P-P-H) idealisation to model the striker-rod impact of cellular materials, but unfortunately, it is not possible to obtain closed-form solutions. A power-law hardening stage has been suggested by Pattofatto et al. [16] to replace the plastic stages of the R-P-P-L idealisation. They derived solutions for the shock strain and the shock speed of a constant-velocity impact scenario.

This paper aims to present general solutions for a unified framework of plastic shock wave models, which may help to obtain high-precision predictions of shock-induced stress enhancement. Shock models are developed by using a constitutive relation with arbitrary plastic hardening for cellular materials and general solutions for two impact scenarios are presented in Section 2. As desired for applications, closed-form/semi-closed-form solutions for a specified idealisation are derived in Section 3. Comparison between the shock models and cell-based finite element models is presented in Section 4, followed by conclusions in Section 5.

2. Continuum-based plastic shock wave models

2.1. Basic equations based on one-dimensional stress wave theory

The constitutive behaviour of cellular materials is considered to be rate-independent, rigid–plastic hardening (R–PH). The stress–strain relation is given by

$$\sigma = \sigma(\varepsilon) \tag{2}$$

with its first derivation $\sigma'(\varepsilon) \geq 0$, which is required as a monotonically increasing function. In this paper, we consider only a plastic shock wave front propagating through a cellular material rod and aim to obtain analytical solutions, especially in closed form, for the plastic shock wave models. Involving the elastic property makes closed-form solutions impossible and does not give much impressive understanding when the impact velocity is not very low, thereby we do not take the elastic property into consideration. One can refer to the work of Lopatnikov et al. [11–13] and Harrigan et al. [18,19] for the influence of the elastic property. Using continuum-based finite element models to consider the influence of the elastic property is also recommended.

The striker-rod impact scenario and the rod-target impact scenario are revisited. The striker mass is M_b and the initial velocity is V_0. The rod with length l_0 and cross-sectional area A_0 is made of a cellular material with density ρ_0. A plastic shock front propagates along the rod, as represented schematically in Fig. 1. At time t, the shock front locates at Lagrangian position $\Phi(t)$ and travels with Lagrangian speed $\dot{\Phi}(t)$, where the dot symbol (.) denotes the derivative with respect to the time. One-dimensional loading and rigid unloading assumptions are adopted here with the continuum-based stress wave theory. The cross-sectional area of the rod is

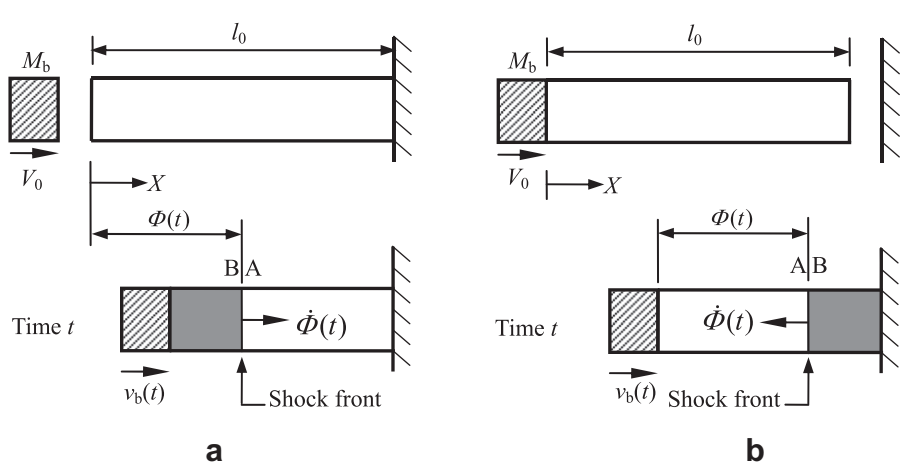

Fig. 1. Schematic diagrams of shock front for (a) the striker-rod impact scenario and (b) the rod-target impact scenario. The location $\Phi(t)$ of the shock front and its speed $\dot{\Phi}(t)$ are measured in the Lagrangian coordinate system.

considered as a constant during the crushing process, so the density ρ at Lagrangian location X after deformation is related to its local strain ε by

$$\rho = \rho_0/(1-\varepsilon). \tag{3}$$

We use $\{v, \varepsilon, \sigma\}$ to list the physical quantities including the particle velocity, strain and stress [10]. Stress and strain are referred to engineering ones and taken as positive in compression. Across the shock front, the physical quantities such as the particle velocity, strain and stress are essentially discontinuous. The jump and the mean of physical quantity Q across the shock front are defined as

$$[Q] = Q_B - Q_A \tag{4}$$

and

$$\langle Q\rangle = (Q_B + Q_A)/2 \tag{5}$$

respectively, where subscripts A and B refer to values closely ahead of and behind the shock front.

Conservation conditions of mass, momentum and energy across the shock front lead to the Rankine–Hugoniot relations [18,20]

$$\begin{cases} [v] = -\rho_0\dot{\Phi}[\rho^{-1}] = \dot{\Phi}[\varepsilon], \\ [\sigma] = \rho_0\dot{\Phi}[v], \\ [U] = -\langle\sigma\rangle[\rho^{-1}] = \rho_0^{-1}\langle\sigma\rangle[\varepsilon], \end{cases} \tag{6}$$

where U is the internal energy per unit mass. It is no need to use the third relation in Eq. (6) as a basic equation in constructing the shock models. A discussion on the energy conservation has been carried out by Harrigan et al. [19]. The first and second relations in Eq. (6) are known as the kinematic and kinetic compatibility conditions across the shock front. Associating these two relations leads to the velocity jump

$$[v] = \pm\sqrt{\frac{1}{\rho_0}[\sigma][\varepsilon]} \tag{7}$$

and the shock speed

$$\dot{\Phi} = \pm\sqrt{\frac{1}{\rho_0}\cdot\frac{[\sigma]}{[\varepsilon]}}, \tag{8}$$

where the plus sign corresponds to a rightward travelling front and the minus sign to a leftward travelling front. A discussion on Eqs. (7) and (8) has been presented by Li and Reid [14]. We use Eqs. (7) and (8) as the basic equations to carry out the present work.

2.2. Solution for the striker-rod impact scenario

For the striker-rod impact scenario, the part of the cellular material behind the shock front travels together with the mass according to the rigid unloading assumption. Their common velocity is denoted as $v_b(t)$. The physical quantities closely ahead of the front (i.e., at Lagrangian location $X_A = \Phi(t)+0$) are $\{v, \varepsilon, \sigma\}_A = \{0, 0, \sigma_0\}$, while those closely behind the front (i.e., at Lagrangian location $X_B = \Phi(t)-0$) are $\{v, \varepsilon, \sigma\}_B = \{v_b(t), \varepsilon_B(t), \sigma_B(t)\}$, in which σ_B is related to ε_B by the stress–strain relation of Eq. (2). Hence, the jumps of physical quantities $\{v, \varepsilon, \sigma\}$ across the shock front are

$$\{[v], [\varepsilon], [\sigma]\} = \{v_b(t), \varepsilon_B(t), \sigma(\varepsilon_B(t)) - \sigma_0\}. \tag{9}$$

Substituting Eq. (9) into Eqs. (7) and (8) with remaining the plus sign due to the convention of the rightward travelling front, one can easily have the expressions for the velocity of the mass and the shock speed related to the unknown strain $\varepsilon_B(t)$, which is determined as follows.

Substituting the initial velocity of the mass $v_b(0) = V_0$ into Eq. (7) with terms in Eq. (9) leads to the following relation

$$(\sigma(\varepsilon_0) - \sigma_0)\varepsilon_0 = \rho_0 V_0^2, \tag{10}$$

where $\varepsilon_0 \equiv \varepsilon_B(0)$ is the initial shock strain. This relation has been obtained by Pattofatto et al. [16] for the case of constant-velocity impact, see Eq. (5a) in Ref. [16]. Here, Eq. (10) is a condition to determine the initial shock strain ε_0 and the corresponding initial shock enhancement is $\sigma(\varepsilon_0) - \sigma_0$. As in the previous work [10], we introduce a dimensionless parameter to characterize the *initial* stress enhancement, namely the stress enhancement parameter,

$$\alpha \equiv \frac{\sigma(\varepsilon_0) - \sigma_0}{\sigma_0} = \frac{\rho_0 V_0^2}{\sigma_0\varepsilon_0}. \tag{11}$$

On the one hand, the acceleration of the mass can be determined by carrying out the differentiation of its velocity with respect to time t, i.e.

$$a_b(t) = \frac{dv_b(t)}{dt} = \frac{\kappa(\varepsilon_B(t))\varepsilon_B(t)}{\rho_0\dot{\Phi}(t)}, \tag{12}$$

where $\kappa(\varepsilon)$ is a combined slope by measuring the average of the slopes of the tangent line (corresponding to the first derivative, $\sigma'(\varepsilon)$) and the Rayleigh line (i.e. the chord line that joins the two stress states $(0, \sigma_0)$ and (ε, σ)) at the point ε on the curve $\sigma(\varepsilon)$,

$$\kappa(\varepsilon) \equiv \frac{1}{2}\left[\sigma'(\varepsilon) + \frac{\sigma(\varepsilon) - \sigma_0}{\varepsilon}\right]. \tag{13}$$

On the other hand, the part of the rod behind the front travels together with the mass, and so according to the inertia law the mass has an acceleration of

$$a_b(t) = -\frac{\sigma_B(t)A_0}{M_b + \rho_0 A_0\Phi(t)} = -\frac{\sigma(\varepsilon_B(t))}{m + \rho_0\Phi(t)}, \tag{14}$$

where m is the specific mass

$$m \equiv M_b/A_0. \tag{15}$$

Eq. (14) also can be derived by applying the momentum conservation, as referred to Refs. [18] and [10].

Combining Eqs. (12) and (14) will lead to a differential equation, see Eq. (B.1). Solving this differential equation with the initial conditions of $\Phi(0) = 0$ and $\varepsilon_B(0) = \varepsilon_0$, we obtain the Lagrangian location of the shock front

$$\Phi(t) = \frac{m}{\rho_0}\left[\exp\left(-\int_{\varepsilon_0}^{\varepsilon_B(t)}\frac{\kappa(\varepsilon)}{\sigma(\varepsilon)}d\varepsilon\right) - 1\right]. \tag{16}$$

From Eq. (16) and Eq. (8), we finally have an implicit solution for $\varepsilon_B(t)$

$$t = -T_1\int_{\varepsilon_0}^{\varepsilon_B(t)}\frac{f_1(\varepsilon)\sqrt{\sigma_0\varepsilon}}{\sqrt{\alpha\varepsilon_0(\sigma(\varepsilon) - \sigma_0)}}d\varepsilon, \tag{17}$$

where T_1 is a characteristic time parameter, defined as

$$T_1 \equiv mV_0/\sigma_0, \tag{18}$$

and f_1 is a dimensionless function, defined as

$$f_1(\varepsilon) = \frac{\kappa(\varepsilon)}{\sigma(\varepsilon)}\exp\left[-\int_{\varepsilon_0}^{\varepsilon}\frac{\kappa(\xi)}{\sigma(\xi)}d\xi\right]. \tag{19}$$

For more details on the derivations, one is referred to Appendix B. The solution in Eq. (17) can be converted to its explicit form of $\varepsilon_B(t)$ for some special constitutive relations, see Section 3.1.

2.3. Solution for the rod-target impact scenario

For the rod-target impact scenario, the part of the cellular material ahead of the shock front travels together with the mass according to the rigid assumption of the elastic behaviour. The physical quantities closely ahead of the front (i.e., at $X_A = \Phi(t) - 0$) are $\{v, \varepsilon, \sigma\}_A = \{v_b(t), 0, \sigma_0\}$ and those closely behind the front (i.e., at $X_B = \Phi(t)+0$) are $\{v, \varepsilon, \sigma\}_B = \{0, \varepsilon_B(t), \sigma(\varepsilon_B(t))\}$, thereby the jumps of physical quantities $\{v, \varepsilon, \sigma\}$ across the shock front are

$$\{[v], [\varepsilon], [\sigma]\} = \{-v_b(t), \varepsilon_B(t), \sigma(\varepsilon_B(t)) - \sigma_0\}. \tag{20}$$

From Eqs. (7) and (8) with remaining the negative sign, one can obtain the expressions for the velocity of the mass and the shock speed related to the unknown strain $\varepsilon_B(t)$. The initial shock strain $\varepsilon_B(0) = \varepsilon_0$ is identical with that from Eq. (10).

Similarly, we can determine the Lagrangian location of the shock front as (see Appendix B)

$$\Phi(t) = \frac{m}{\rho_0}\left[(1+\mu)\exp\left(\int_{\varepsilon_0}^{\varepsilon_B(t)}\frac{\kappa(\varepsilon)}{\sigma_0}d\varepsilon\right) - 1\right], \tag{21}$$

where μ is the ratio of the rod's mass to the striker mass

$$\mu \equiv \rho_0 l_0 A_0 / M_b = \rho_0 l_0 / m. \tag{22}$$

From Eq. (21) and Eq. (8), as derived in Appendix B, we finally have an implicit solution for $\varepsilon_B(t)$

$$t = -T_2\int_{\varepsilon_0}^{\varepsilon_B(t)}\frac{f_2(\varepsilon)\sqrt{\sigma_0\varepsilon}}{\sqrt{\alpha\varepsilon_0(\sigma(\varepsilon)-\sigma_0)}}d\varepsilon, \tag{23}$$

where T_2 and f_2 are defined by

$$T_2 \equiv (m + \rho_0 l_0)V_0/\sigma_0 = T_1(1+\mu) \tag{24}$$

and

$$f_2(\varepsilon) = \frac{\kappa(\varepsilon)}{\sigma_0}\exp\left(\int_{\varepsilon_0}^{\varepsilon}\frac{\kappa(\xi)}{\sigma_0}d\xi\right), \tag{25}$$

respectively. Few constitutive relations can make Eq. (23) convert to its explicit form of $\varepsilon_B(t)$, so we will focus only on its semi-closed-form solutions, see Section 3.2.

2.4. A discussion on the general solutions

General solutions of $\varepsilon_B(t)$, although implicit, have been derived for the two impact scenarios with an arbitrary plastic hardening constitutive relation of cellular material. For the striker-rod impact scenario, the strain behind the shock front $\varepsilon_B(t)$ is related to t by Eq. (17), while for the rod-target impact scenario, it is related to t by Eq. (23). These two relations are identical in the form but different in the definitions of $f_i(\varepsilon)$ and T_i, $i = 1, 2$. The functions $f_1(\varepsilon)$ and $f_2(\varepsilon)$ are defined in Eqs. (19) and (25), respectively. They are dependent on the constitutive relation of cellular materials. The time parameters T_1 and T_2 are defined in Eqs. (18) and (24), respectively. The time parameters characterize the ratios of the initial momentum of the system per unit area to the yield stress of the rod. General solutions for the plate impact and the Taylor impact can then be determined, since they are equivalent to the striker-rod impact with $l_0 \to \infty$ and the rod-target impact with $M_b = 0$, respectively.

The initial solution of the shock strain ε_0 is identical for all of the impact scenarios mentioned above, which depends on the initial impact velocity but not the striker mass. At the initial stage of impact, we present the first-order asymptotic solutions as

$$\begin{cases} \varepsilon_B(t) = \varepsilon_0 - \dfrac{\sigma(\varepsilon_0)}{\kappa(\varepsilon_0)}\cdot\dfrac{\alpha t}{T_1} + O\left[\left(\dfrac{\alpha t}{T_1}\right)^2\right] \\ \sigma_B(t) = \sigma(\varepsilon_0) - \dfrac{\sigma'(\varepsilon_0)\sigma(\varepsilon_0)}{\kappa(\varepsilon_0)}\cdot\dfrac{\alpha t}{T_1} + O\left[\left(\dfrac{\alpha t}{T_1}\right)^2\right] \end{cases} \tag{26}$$

for the striker-rod impact scenario and

$$\begin{cases} \varepsilon_B(t) = \varepsilon_0 - \dfrac{\sigma_0}{\kappa(\varepsilon_0)}\cdot\dfrac{\alpha t}{T_2} + O\left[\left(\dfrac{\alpha t}{T_2}\right)^2\right] \\ \sigma_B(t) = \sigma(\varepsilon_0) - \dfrac{\sigma'(\varepsilon_0)\sigma_0}{\kappa(\varepsilon_0)}\cdot\dfrac{\alpha t}{T_2} + O\left[\left(\dfrac{\alpha t}{T_2}\right)^2\right] \end{cases} \tag{27}$$

for the rod-target impact scenario.

3. Application to a special constitutive relation

The shock models may have simple solutions for some special constitutive relations, such as the R-P-P-L idealisation and the R-LHP-L idealisation [10]. Here, a particular type of constitutive relation was employed to obtain some closed-form/semi-closed-form solutions. The shock models for the two impact scenarios are related to the combined slope defined in Eq. (13). For convenience, we consider the slope of the tangent line at the point ε on the curve $\sigma(\varepsilon)$ proportional to the slope of the Rayleigh line, denoted by

$$\sigma'(\varepsilon) = n(\sigma(\varepsilon) - \sigma_0)/\varepsilon, \tag{28}$$

where n is the proportionality coefficient ($n \geq 1$). Thus, the combined slope defined in Eq. (13) can be simplified as

$$\kappa(\varepsilon) = q\sigma'(\varepsilon), \tag{29}$$

where q is related to n by

$$q \equiv (n+1)/2n. \tag{30}$$

As $n \geq 1$, we have $1/2 \leq q \leq 1$. From Eqs. (16) and (21) with Eq. (29), the locations of the front in the two impact scenarios can be integrated as

$$\Phi(t) = \frac{m}{\rho_0}\left[\left(\frac{\sigma(\varepsilon_B(t))}{\sigma(\varepsilon_0)}\right)^{-q} - 1\right] \tag{31}$$

and

$$\Phi(t) = \frac{m}{\rho_0}\left[(1+\mu)\exp\left(\frac{q}{\sigma_0}(\sigma(\varepsilon_B(t)) - \sigma(\varepsilon_0))\right) - 1\right], \tag{32}$$

respectively. Solving the simple differential equation Eq. (28) with $\sigma(0) = \sigma_0$, we are led to a constitutive relation, namely the rigid–power-law hardening (R-PLH) idealisation

$$\sigma(\varepsilon) = \sigma_0 + K\varepsilon^n, \tag{33}$$

where σ_0 is the yield stress, K the strength index and n the strain-hardening index. Pattofatto et al. [16] have used this constitutive model instead of the R-P-P-L idealisation to improve the predictions of the shock strain and the shock speed for the case of constant-velocity impact. In this paper, we focus on the case of initial-velocity impact. The shock strain predicted by Pattofatto et al. [16] is equivalent to the *initial* shock strain of the present work, which is written as

$$\varepsilon_0 = \left(\rho_0 V_0^2/K\right)^{1/(n+1)}. \tag{34}$$

This strain can be easily determined by substituting Eq. (33) into Eq. (10). The *initial* shock stress is determined as

$$\sigma(\varepsilon_0) = \sigma_0 + K\left(\rho_0 V_0^2/K\right)^{n/(n+1)}. \tag{35}$$

Thus, the stress–enhancement parameter can be given by

$$\alpha = K\varepsilon_0^n/\sigma_0 = \left(K\left(\rho_0 V_0^2\right)^n\right)^{1/(n+1)} \Big/ \sigma_0. \tag{36}$$

Solutions for the two impact scenarios are derived as follows.

3.1. The striker-rod impact scenario

3.1.1. Closed-form solutions

Substituting Eqs. (29) and (33) into Eq. (19), we obtain

$$f_1(\xi) = \frac{nq}{\varepsilon_0}\cdot\frac{\alpha(1+\alpha)^q(\xi/\varepsilon_0)^{n-1}}{\left[1+\alpha\left(\frac{\xi}{\varepsilon_0}\right)^n\right]^{q+1}}, \tag{37}$$

where q is defined in Eq. (30), which is an equivalent strain-hardening index. Hence, Eq. (17) can be given in the form

$$t = -T_1\frac{nq}{\varepsilon_0}(1+\alpha)^q\int_{\varepsilon_0}^{\varepsilon_B}\frac{\left(\frac{\varepsilon}{\varepsilon_0}\right)^{(n-1)/2}}{\left[1+\alpha\left(\frac{\varepsilon}{\varepsilon_0}\right)^n\right]^{q+1}}\mathrm{d}\varepsilon. \tag{38}$$

By taking $\eta = (\varepsilon/\varepsilon_0)^{-n}$, Eq. (38) can be simplified as

$$t = T_1 q(1+\alpha)^q\int_1^{(\varepsilon_B/\varepsilon_0)^{-n}}(\eta+\alpha)^{-q-1}\mathrm{d}\eta. \tag{39}$$

Carrying out the definite integral in Eq. (39), we finally have

$$t = T_1\left[1-\left(\frac{1+\alpha}{(\varepsilon_B/\varepsilon_0)^{-n}+\alpha}\right)^q\right]. \tag{40}$$

This equation is an implicit form of ε_B with respect to time t, but it can be easily converted to the explicit form. Thus, we have the strain and stress closely behind the front

$$\varepsilon_B(t) = \varepsilon_0\left[(1+\alpha)(1-t/T_1)^{-1/q}-\alpha\right]^{-1/n}. \tag{41}$$

and

$$\sigma_B(t) = \sigma_0(1+\alpha)\left[1+\alpha-\alpha(1-t/T_1)^{\frac{1}{q}}\right]^{-1}, \tag{42}$$

respectively. From Eqs. (7), (9) and (12), the velocity and acceleration of the mass can be determined as

$$v_b(t) = V_0\left[(1+\alpha)(1-t/T_1)^{-1/q}-\alpha\right]^{-q}. \tag{43}$$

and

$$a_b(t) = -\frac{\sigma_0}{m}(1+\alpha)\left[1+\alpha-\alpha(1-t/T_1)^{1/q}\right]^{-q-1}, \tag{44}$$

respectively. From Eqs. (B.3) and (31), the speed and location of the front can be given by

$$\dot{\Phi}(t) = \frac{V_0}{\varepsilon_0}\left[(1+\alpha)(1-t/T_1)^{-1/q}-\alpha\right]^{q-1}. \tag{45}$$

and

$$\Phi(t) = \frac{m}{\rho_0}\left[\left(1+\alpha-\alpha(1-t/T_1)^{1/q}\right)^q-1\right], \tag{46}$$

respectively.

3.1.2. Some transition parameters

The deformation patterns of a cellular material under different impact velocities are very different, which has been catalogued into three deformation modes: a Homogeneous Mode, a Transitional Mode and a Shock Mode [8,9,21]. There exist two critical impact velocities: the first critical velocity, V_{c1}, which corresponds to the mode transition between the Homogeneous and the Transitional modes, and the second critical velocity, V_{c2}, which corresponds to the mode transition between the Transitional and the Shock modes. A stress uniformity index (SUI), defined as the ratio of the plateau stresses at the support and the impact ends, has been introduced to determine the first critical velocity when SUI = 90% for constant-velocity impact [21,22]. Here, at the initial stage of crushing, the stress at the support end is σ_0 and the stress at the impact end is $\sigma(\varepsilon_0)$ as given in Eq. (35). Hence, from $\sigma_0/\sigma(\varepsilon_0) = 90\%$ with $V_0 = V_{c1}$, we obtain the first critical velocity

$$V_{c1} = \left(\frac{\sigma_0}{9K}\right)^{(n+1)/2n}\sqrt{K/\rho_0}. \tag{47}$$

The second critical velocity can be determined by the fact when the shock strain reaches the densification strain [10]. From Eq. (34) with $\varepsilon_0 = \varepsilon_D$ and $V_0 = V_{c2}$, we have

$$V_{c2} = \varepsilon_D^{(n+1)/2}\sqrt{K/\rho_0}. \tag{48}$$

When the initial impact velocity is very high and the rod is long enough, both mode transitions occur during the crushing process. The deformation mode changes from the Shock Mode to the Transitional Mode at time t_{S-T}, which is determined from Eq. (43) when $v_b(t_{S-T}) = V_{c2}$, i.e.

$$t_{S-T} = T_1\left[1-\left(\frac{1+1/\alpha}{1+1/\beta}\right)^q\right], \tag{49}$$

where $\beta = K\varepsilon_D^n/\sigma_0$. The deformation mode changes from the Transitional Mode to the Homogeneous Mode at time $t_{T\text{-}H}$, which is determined from Eq. (43) when $v_b(t_{T-H}) = V_{c1}$, i.e.

$$t_{T-H} = T_1\left[1-(0.1(1+1/\alpha))^q\right]. \tag{50}$$

According to this shock model, when the rod is long enough, the striker will stop at time $t_{end} = T_1$ since $v_b(T_1) = 0$. Therefore, the time parameter T_1 characterises the time when the kinetic energy of the mass converts totally to the internal energy of the rod. It is interesting that t_{end} does not depend on the hardening parameters except of the yield stress. At this time, the location of the front is

$$\Phi(t_{end}) = \frac{m}{\rho_0}\left[(1+\alpha)^q - 1\right], \tag{51}$$

and so $l_0 \geq \Phi(t_{end})$ as required. However, if the rod is not long enough, i.e. $l_0 < \Phi(t_{end})$, the front will be reflected from the distal end at time

$$t_1 = T_1\left[1-\left(1+\alpha^{-1}-\alpha^{-1}(1+\mu)^{\frac{1}{q}}\right)^q\right], \tag{52}$$

which is derived from $\Phi(t_1) = l_0$. The case of wave reflection has not been considered in this paper, but it can be extended, as presented in Ref. [10].

3.1.3. Limit cases of the strain-hardening index

For the case of $n = 1$, we have $q = 1$ and $K = E_1$ with E_1 being the plastic hardening modulus. Eqs. (41)–(43) lead to

$$\begin{cases} \varepsilon_B(t) = \varepsilon_0(1-t/T_1)(1+\alpha t/T_1)^{-1} \\ \sigma_B(t) = \sigma_0(1+\alpha)(1+\alpha t/T_1)^{-1} \\ v_b(t) = V_0(1-t/T_1)(1+\alpha t/T_1)^{-1} \end{cases}, \tag{53}$$

where $\varepsilon_0 = V_0/C_1$ and $\alpha = \rho_0 C_1 V_0/\sigma_0$ with $C_1 = (E_1/\rho_0)^{1/2}$ being the plastic wave speed. These results have been predicted in Ref. [10] for the R-LHP-L idealisation subjected to the mass impact with a moderate initial velocity.

For the case of $n \to \infty$, we obtain $q = 1/2$. The strain closely behind the front reaches the densification strain, i.e. $\varepsilon_B(t) = \varepsilon_0 = \varepsilon_D$. Eqs. (42) and (43) lead to

$$\begin{cases} \sigma_B(t) = \sigma_0(1+\alpha)\left[1+\alpha-\alpha(1-t/T_1)^2\right]^{-1} \\ v_b(t) = V_0(1-t/T_1)\left[1+\alpha-\alpha(1-t/T_1)^2\right]^{-1/2} \end{cases}, \tag{54}$$

where $\alpha = \rho_0 V_0^2/(\sigma_0\varepsilon_D)$. These predictions are valid for both the R-P-P-L and the R-LHP-L idealisations when the impact velocity is very high, as discussed in Ref. [10]. It should be noticed that the corresponding predictions in the original R-P-P-L shock model [1,4] are expressed in implicit form.

Therefore, the predictions involved in the R-P-P-L and the R-LHP-L idealisations can be easily deduced from the present limit cases of the strain-hardening index. The related critical velocities of modes transition have been discussed in Ref. [10].

3.2. The rod-target impact scenario

3.2.1. Semi-closed-form solutions

Similarly, substituting Eqs. (33) and (29) into Eq. (25), we have

$$f_2(\xi) = \frac{\alpha q n}{\varepsilon_0}\exp\left[\alpha q\left(\left(\frac{\xi}{\varepsilon_0}\right)^n - 1\right)\right]\left(\frac{\xi}{\varepsilon_0}\right)^{n-1}, \tag{55}$$

where q is defined in Eq. (30). Thus, Eq. (23) can be expressed by

$$t = -T_2\frac{nq}{\varepsilon_0}\int_{\varepsilon_0}^{\varepsilon_B(t)}\exp\left[\alpha q\left(\left(\frac{\varepsilon}{\varepsilon_0}\right)^n - 1\right)\right]\left(\frac{\varepsilon}{\varepsilon_0}\right)^{\frac{(n-1)}{2}}d\varepsilon. \tag{56}$$

by taking $u = \alpha q(\varepsilon/\varepsilon_0)^n$, the above equation can be rewritten as

$$t = -\frac{T_2}{\alpha(\alpha q)^{q-1}e^{\alpha q}}\int_{\alpha q}^{\alpha q(\varepsilon_B/\varepsilon_0)^n} u^{q-1}e^u du, \tag{57}$$

or in the form

$$t = \frac{T_2}{\alpha(\alpha q)^{q-1}e^{\alpha q}}\left[F(q,\alpha q) - F\left(q,\alpha q\left(\frac{\varepsilon_B}{\varepsilon_0}\right)^n\right)\right], \tag{58}$$

where $F(q, \zeta)$ is a function defined by

$$F(q,\zeta) \equiv \int_0^{\zeta} u^{q-1}e^u du \tag{59}$$

with its first derivative

$$F'(q,\zeta) = \frac{d}{d\zeta}F(q,\zeta) = \zeta^{q-1}e^{\zeta}. \tag{60}$$

the function $F(q, \zeta)$ may have some closed-form solutions, for example $F(1, \zeta) = e^{\zeta} - 1$. Let

$$s \equiv F(q,\alpha q) - \alpha(\alpha q)^{q-1}e^{\alpha q}t/T_2, \tag{61}$$

Eq. (58) can be rewritten as

$$F\left(q,\alpha q\left(\frac{\varepsilon_B}{\varepsilon_0}\right)^n\right) = s, \tag{62}$$

so we have the strain closely behind the front

$$\varepsilon_B(t) = \varepsilon_0\left(\frac{F^{-1}(q,s)}{\alpha q}\right)^{\frac{1}{n}}, \tag{63}$$

where $F^{-1}(q, s)$ is the inverse of the function $F(q, \zeta)$, for example $F^{-1}(1, s) = \ln(1 + s)$. The function $F^{-1}(q, s)$ can not be expressed in a closed form for almost all values of q, but it can be easily determined by solving $F(q, \zeta) = s$ for ζ through Newton's method with the iterative formula

$$\zeta_k = \zeta_{k-1} + \frac{s - F(q,\zeta_{k-1})}{F'(q,\zeta_{k-1})}, \quad k = 1, 2, \ldots, \tag{64}$$

where ζ_0 is a first guess value. By substituting Eq. (63) into Eq. (33), the stress closely behind the front is given by

$$\sigma_B(t) = \sigma_0\left(1 + F^{-1}(q,s)/q\right). \tag{65}$$

Thus, the shock speed and the velocity of the mass can be expressed by

$$\dot{\Phi}(t) = -\frac{V_0}{\varepsilon_0}\left(\frac{F^{-1}(q,s)}{\alpha q}\right)^{1-q} \tag{66}$$

and

$$v_b(t) = V_0\left(\frac{F^{-1}(q,s)}{\alpha q}\right)^{q}, \tag{67}$$

respectively. The location of the shock front Eq. (32) is determined as

$$\Phi(t) = \frac{m}{\rho_0}\left[(1+\mu)\exp\left(F^{-1}(q,s) - \alpha q\right) - 1\right] \tag{68}$$

and then the acceleration of the mass Eq. (B.7) is given by

$$a_b(t) = -\frac{\sigma_0}{m(1+\mu)}\exp\left(-F^{-1}(q,s) + \alpha q\right). \tag{69}$$

3.2.2. Some transition parameters

The two critical impact velocities presented in Eqs. (47) and (48) are also adequate for the rod-target impact scenario. Mode transitions may occur during the crushing process when the initial impact velocity is very high and the rod is long enough. The time of mode transition from the Shock Mode to the Transitional Mode is determined from Eq. (67) when $v_b(t_{S-T}) = V_{c2}$, i.e.

$$t_{S-T} = T_2\frac{F(q,\alpha q) - F(q,\beta q)}{\alpha(\alpha q)^{q-1}e^{\alpha q}}, \tag{70}$$

where $\beta = K\varepsilon_D^n/\sigma_0$. The time of mode transition from the Transitional Mode to the Homogeneous Mode is determined from Eq. (67) when $v_b(t_{T-H}) = V_{c1}$, i.e.

$$t_{T-H} = T_2\frac{F(q,\alpha q) - F(q,q/9)}{\alpha(\alpha q)^{q-1}e^{\alpha q}}. \tag{71}$$

If the rod is long enough, from Eq. (67) with $v_b(t_{end}) = 0$, we can determine the time t_{end} when the crushing stops, i.e.

$$t_{end} = T_2\frac{F(q,\alpha q)}{\alpha(\alpha q)^{q-1}e^{\alpha q}}. \tag{72}$$

Given n or q, the dimensionless time t_{end}/T_2 reduces with increasing the stress–enhancement parameter α. Different from that of the striker-rod impact scenario, the time t_{end} in the present impact scenario is related to all the hardening parameters including the yield stress, the strength index and the strain-hardening index. At time t_{end}, the location of the front is

$$\Phi(t_{end}) = \frac{m}{\rho_0}\left[(1+\mu)e^{-\alpha q} - 1\right]. \tag{73}$$

when $\Phi(t_{end}) \geq 0$, i.e. $l_0 \geq (e^{\alpha q} - 1)m/\rho_0$, the rod is long enough. However, if the rod is not long enough, the front will be reflected from the distal end at time t_1,

$$t_1 = \frac{F(q,\alpha q) - F(q,\alpha q - \ln(1+\mu))}{\alpha(\alpha q)^{q-1}e^{\alpha q}}T_2, \tag{74}$$

which is derived from $\Phi(t_1) = 0$.

3.2.3. Limit cases of the strain-hardening index

For the case of $n = 1$, we have $q = 1$ and $K = E_1$. Since $F(1,\zeta) = e^{\zeta} - 1$, Eq. (61) gives

$$s = e^{\alpha} - 1 - \alpha e^{\alpha}t/T_2, \tag{75}$$

and so we obtain

$$F^{-1}(1,s) = \ln(1+s) = \alpha + \ln(1 - \alpha t/T_2), \tag{76}$$

where $\alpha = \rho_0 C_1 V_0/\sigma_0$. Eqs. (63), (65) and (67) lead to closed-form expressions

$$\begin{cases} \varepsilon_B(t) = \varepsilon_0\left[1 + \alpha^{-1}\ln(1 - \alpha t/T_2)\right] \\ \sigma_B(t) = \sigma_0\left[1 + \alpha + \ln(1 - \alpha t/T_2)\right] \\ v_b(t) = V_0\left[1 + \alpha^{-1}\ln(1 - \alpha t/T_2)\right] \end{cases}, \tag{77}$$

where $\varepsilon_0 = V_0/C_1$. These results correspond to Eqs. (2), (5) and (6) in Ref. [10].

For the case of $n \to \infty$, we obtain $q = 1/2$. Since

$$F\left(\frac{1}{2},\zeta\right) = -\sqrt{\pi}\cdot i\cdot \mathrm{erf}\left(i\sqrt{\zeta}\right) = \sqrt{\pi}\cdot \mathrm{erfi}\left(\sqrt{\zeta}\right), \tag{78}$$

where i is the imaginary unit, erf the error function and erfi the imaginary error function with

$$\mathrm{erf}(\xi) \equiv \frac{2}{\sqrt{\pi}}\int_0^{\xi} e^{-u^2}du \tag{79}$$

and

$$\mathrm{erfi}(\eta) = -i\cdot\mathrm{erf}(i\eta), \tag{80}$$

Eq. (61) gives $s = \tau\sqrt{\pi}$ with

$$\tau = \mathrm{erfi}\left(\sqrt{\alpha/2}\right) - \sqrt{2\alpha e^{\alpha}/\pi}\, t/T_2, \tag{81}$$

where $\alpha = \rho_0 V_0^2/(\sigma_0\varepsilon_D)$. Solving $F(1/2,\zeta) = s$, which can be simplified as $\mathrm{erfi}(\sqrt{\zeta}) = \tau$, for ζ, we have

$$F^{-1}\left(\frac{1}{2},s\right) = \zeta = \left(\mathrm{erfi}^{-1}(\tau)\right)^2. \tag{82}$$

The inverse of the imaginary error function $\mathrm{erfi}^{-1}(\tau)$ can be determined by solving $\mathrm{erfi}(\xi) = \tau$ for ξ through Newton's method with the iterative formula

$$\xi_k = \xi_{k-1} + \frac{\tau - \mathrm{erfi}(\xi_{k-1})}{\left(2/\sqrt{\pi}\right)e^{\xi_{k-1}^2}}, \quad k = 1,2,\ldots, \tag{83}$$

where ξ_0 is a first guess value. The strain closely behind the front reaches the densification strain, i.e. $\varepsilon_B(t) = \varepsilon_0 = \varepsilon_D$. Eqs. (65) and (67) lead to

$$\begin{cases} \sigma_B(t) = \sigma_0\left[1 + 2\left(\mathrm{erfi}^{-1}(\tau)\right)^2\right] \\ v_b(t) = V_0\sqrt{\frac{2}{\alpha}}\cdot\mathrm{erfi}^{-1}(\tau) \end{cases}, \tag{84}$$

which have also been predicted in Ref. [10].

4. Comparisons with cell-based finite element simulations

Two types of virtual cellular structures are employed to demonstrate the validity of the continuum-based shock models. One type is an irregular honeycomb and the other is a closed-cell foam. They are constructed by the 2D and 3D random Voronoi techniques, respectively. The 2D Voronoi method was introduced in Ref. [8] and the 3D Voronoi method was introduced in Ref. [23]. The methods are briefly introduced here with four steps. Step 1, N nuclei are randomly generated in a given region (an area or a box) by constraining the minimum allowable distance between any two nuclei. Step 2, the nuclei are copied to the surrounding neighbouring regions by transitions. Step 3, the Delaunay triangulation and the Voronoi diagram are constructed. Step 4, the part of the Voronoi diagram in the given region is reserved to form the desired specimen.

The quasi-static compression and the dynamic impact of specimens were implemented by the finite element (FE) simulations using ABAQUS/Explicit code. The specimens are sandwiched between two rigid platens. One platen is fixed and the other moves along the x-direction. Cell walls of specimens are modelled with shell elements as used in Refs. [8] and [23]. Contact with a slight friction is specified between any possible surfaces.

The irregular honeycomb and the closed-cell foam used in this paper have the relative density of 0.1 and the cell irregularity of 0.5. The specimen of honeycomb for quasi-static compression is constructed in an area of 100 mm × 100 mm with 400 nuclei (the length of specimen in the out-of-plane direction is 1 mm), while that of foam is constructed in a box of 25 mm × 25 mm × 25 mm with 400 nuclei. The geometric dimensions of specimens for dynamic impact are given later, which have the same number densities of nucleation. The average cell size of the honeycomb is about 5.4 mm and that of the foam is about 4.1 mm. The cell-wall thickness of the honeycomb is about 0.254 mm and that of the foam is about 0.130 mm. The average element length of the honeycomb is about 0.5 mm and that of the foam is about 0.6 mm. The cell-wall material of all specimens is taken to be elastic-perfectly plastic with Young's modulus, yield stress, Possion's ratio and mass density being 69 GPa, 170 MPa, 0.3 and 2700 kg/m^3, respectively. The friction coefficient is set to be 0.02.

The quasi-static stress–strain curves for the two types of cellular materials and the corresponding idealisations are shown in Fig. 2. In Fig. 2a, the material parameters of the irregular honeycomb are presented here: $\sigma_{pl} = 0.862$ MPa and $\varepsilon_L = 0.579$ for the R-P-P-L idealisation; $\sigma_0 = 0.668$ MPa, $E_1 = 0.981$ MPa and $\varepsilon_L = 0.579$ for the R-LHP-L idealisation; $\sigma_0 = 0.668$ MPa, $K = 12.72$ MPa and $n = 5.69$ for the R-PLH idealisation. In Fig. 2b, the material parameters for the closed-cell foam are presented as follows: $\sigma_{pl} = 7.39$ MPa and $\varepsilon_L = 0.623$ for the R-P-P-L idealisation; $\sigma_0 = 6.19$ MPa, $E_1 = 5.23$ MPa and $\varepsilon_L = 0.623$ for the R-LHP-L idealisation; $\sigma_0 = 6.19$ MPa, $K = 50.2$ MPa and $n = 5.68$ for the R-PLH idealisation. The locking strain ε_L is assumed to be equal to the densification strain ε_D, which corresponds to the maximum of the energy absorption efficiency [24,25]. Some parameters here are estimated because of the oscillation of the numerical FE results. The yield strain is taken as 0.01 and the yield stress σ_0 is estimated near this strain. The plateau stress σ_{pl} is calculated from the average stress over the strain range of 0.01 to ε_D. The strength index K and the strain-hardening index n are determined by the method of least squares. The hardening modulus E_1 is determined as $(\sigma_D - \sigma_0)/\varepsilon_D$, in which $\sigma_D = \sigma(\varepsilon_D)$ is estimated from the R-PLH idealisation. These parameters are used in the following comparisons.

Two dynamic impact cases are considered in this section. Case 1, an irregular honeycomb is stationary with a fixed rigid wall at its right end, while another rigid wall with mass $M_b = 5$ g and initial velocity $V_0 = 100$ m/s comes from the left end of the honeycomb. The size of the honeycomb is 400 mm × 100 mm × 1 mm. In this simulation case, the number of nodes is 54754 and the number of elements is 28,840. Case 2, a closed-cell foam with a rigid wall ($M_b = 31.25$ g) at its left end travels at an initial velocity of $V_0 = 100$ m/s and strikes axially against a fixed rigid wall at its right end. The size of the foam is 100 mm × 25 mm × 25 mm. In this case, the number of nodes is 138,153 and the number of elements is 172,525. The dynamic impact is along the longest dimension of each specimen. Force responses and deformation features are presented below.

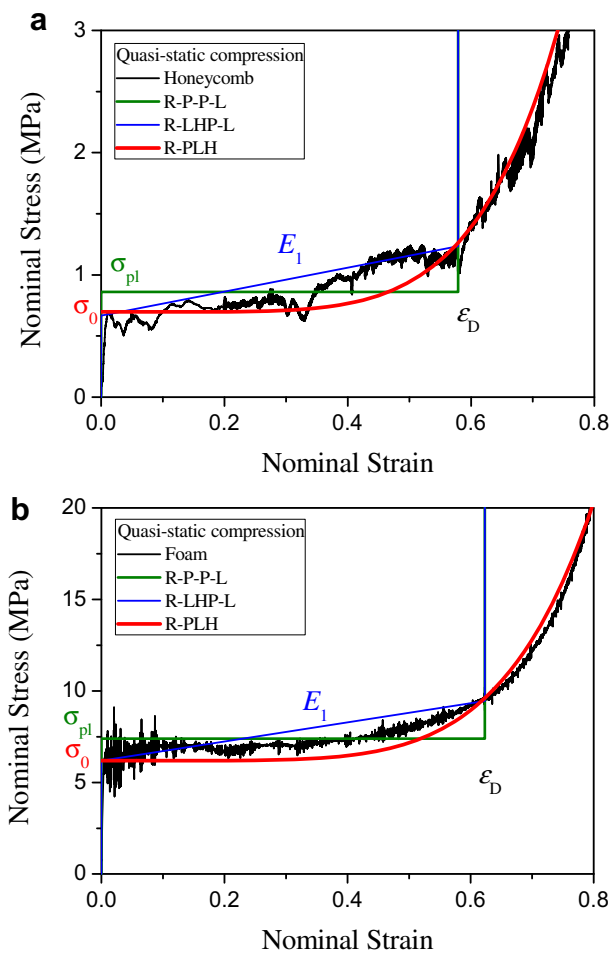

Fig. 2. The quasi-static stress–strain relations with three different idealisations for two types of cellular materials: (a) The irregular honeycomb and (b) the closed-cell foam.

4.1. Case 1: A striker-rod impact of an irregular honeycomb

4.1.1. Force responses

The forces detected at the two ends of the honeycomb specimen are shown in Fig. 3. The numerical FE results show that at the initial stage of crushing, the force at the left end of the specimen is much larger than that at the right end, which was well known as the strength enhancement. During the crushing process, the amplitude of the force at the left end reduces rapidly, but the force at the right end almost remains at a stable level. From the shock models, the force response at the left end of the specimen is given by

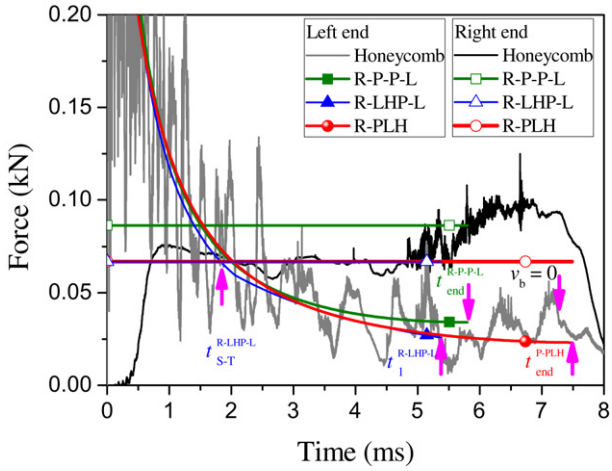

Fig. 3. Forces at the two ends of the irregular honeycomb under dynamic impact versus the impact time.

$$F_{\text{left}} = -M_b a_b = \frac{mA_0\sigma_B(t)}{m + \rho_0\Phi(t)} \tag{85}$$

and the one at the right end of the specimen is written as

$$F_{\text{right}} = A_0\sigma_A(t), \tag{86}$$

which are also shown in Fig. 3. The force at the left end of the specimen given in Eq. (85) is determined by considering the motion governed by the inertia law. This is reasonable because we have taken into account the influence of the unloading wave behind the shock front and given up the assumption used by Tan et al. [4], who assumed only two stress states in the specimen. The comparison shows that the theoretical predictions are in good agreement with the numerical FE results. The force responses are not very sensitive to the choice of the idealisations, but the deformation features may be very different when using different idealisations. The R-PLH model predicts that the mass stops at time $t_{\text{end}} = 7.49$ ms, which is close to the numerical FE result, i.e. 7.265 ms.

4.1.2. Deformation features

Some deformation patterns of the irregular honeycomb under crushing are shown in Fig. 4. The deformation localisation is observed in the specimen. Cells collapse layer-by-layer and a deformation front propagates from the left end to the right end of the specimen, see the pattern at $t = 1$ ms. As the impact energy is absorbed by the collapsed cells, the impact velocity of the mass is reduced. When this velocity is not very high, cells are not fully collapsed (see the pattern at $t = 2.2$ ms, which corresponds to $v_b = 38.2$ m/s) and then deformation bands are random (see the pattern at $t = 5.4$ ms, which corresponds to $v_b = 10.8$ m/s).

To characterise the deformation features, we employed the discrete deformation gradient [26,27] to determine the local strain in the X-direction, see Appendix C. The local engineering strain fields corresponding to the above deformation patterns are also shown in Fig. 4. It should be noticed that this local strain is resulted from statistical average with measuring over the range of 1.5 times of cell size. The strain field at $t = 1$ ms shows that the shock front is macroscopic even and there is almost no deformation ahead of the shock front. The strain field at $t = 2.2$ ms shows that the shock front turns not very even. This is due to the influence of the irregularity of cells when the impact velocity is not high. At $t = 5.4$ ms, the large strain locals at random deformation bands. Based on the one-dimensional assumption, the local strain at location X is defined as the average strain along the Y-direction. An example of the strain distribution along the X-direction is shown in Fig. 5a, which corresponds to the time when the mass has zero velocity ($t_{\text{end}} = 7.265$ ms). The magnitude of the strain reduces along the X-direction. The strain distributions predicted by the shock models are plotted also in Fig. 5a. The R-P-P-L model predicts $t_{\text{end}} = 5.80$ ms and the R-PLH model predicts $t_{\text{end}} = 7.49$ ms that the shock front has not reached the right end of the specimen. However, the R-LHP-L model predicts the front reaches the right end of the specimen at time $t_1 = 5.39$ ms. Compared to the numerical FE result, the strain distribution has been well predicted by the shock models. The comparison also shows that using more realistic constitutive model such as the R-PLH idealisation has more accurate predictions. The strain distributions at different times predicted by the cell-based FE model and the R-PLH model

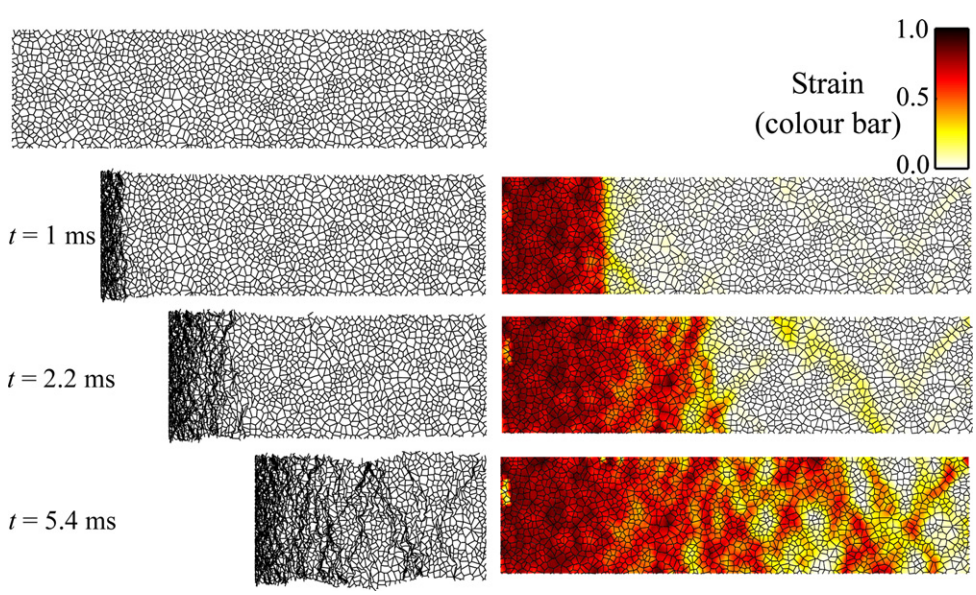

Fig. 4. Deformation patterns (left column) and their corresponding local strain fields in the Lagragian coordinate system (right column) for the irregular honeycomb under dynamic impact.

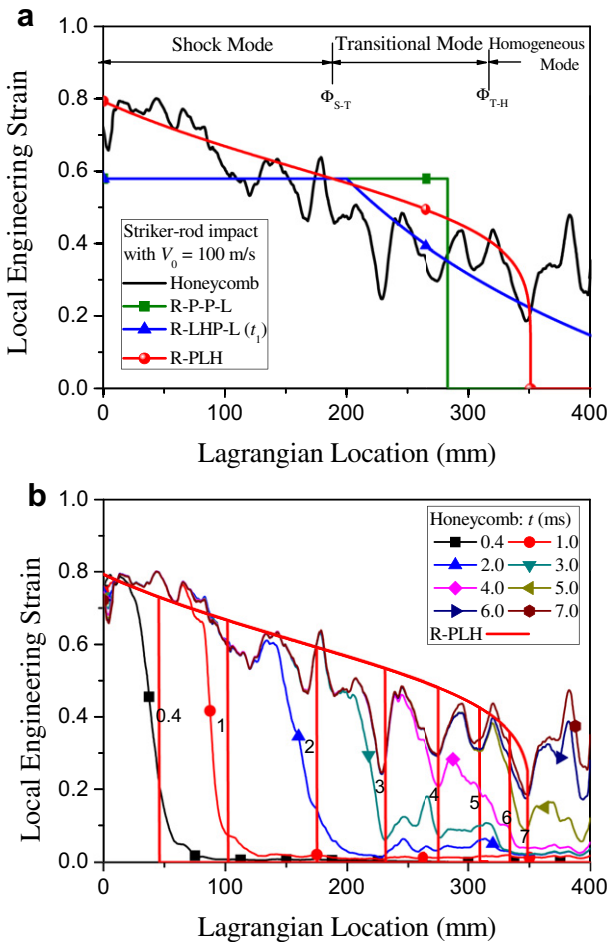

Fig. 5. Local strain distributions along the *X*-direction of the irregular honeycomb: (a) when the striker stops and (b) at different times.

are plotted in Fig. 5b. The shock fronts obtained from the cell-based model seem not as steep as those from the shock models, but concerning about this difference has no substantive significance. The difference is due to the mathematical treatments. On one hand, the cell size in the cell-based model is an intrinsic length

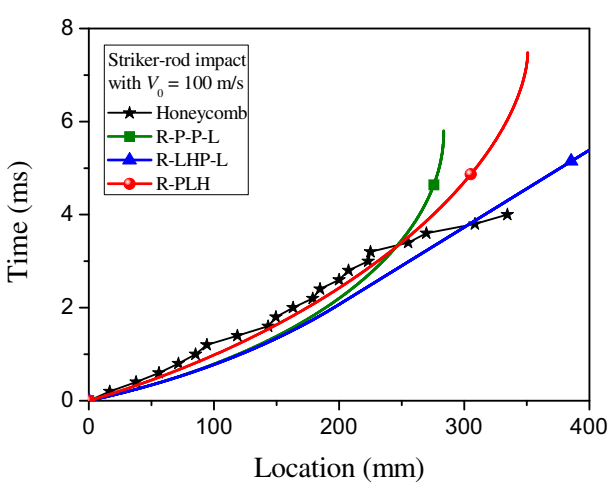

Fig. 6. The impact time versus the Lagrangian location of shock front in the striker-rod impact scenario of the irregular honeycomb.

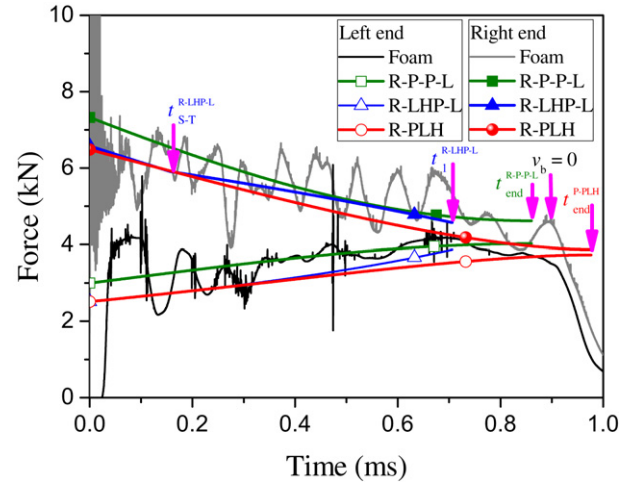

Fig. 7. Forces at the two ends of the closed-cell foam under dynamic impact versus the impact time.

scale, the physical quantities below this scale are macroscopically meaningless and not reasonable. On the other hand, there is no intrinsic length scale in the continuum-based shock models and so the jump across the shock front is described as a mathematical discontinuity. The magnitude of the strain behind the front reduces as the impact time increases. The strain ahead of the front becomes apparent after 3 ms, which is because of the influence of

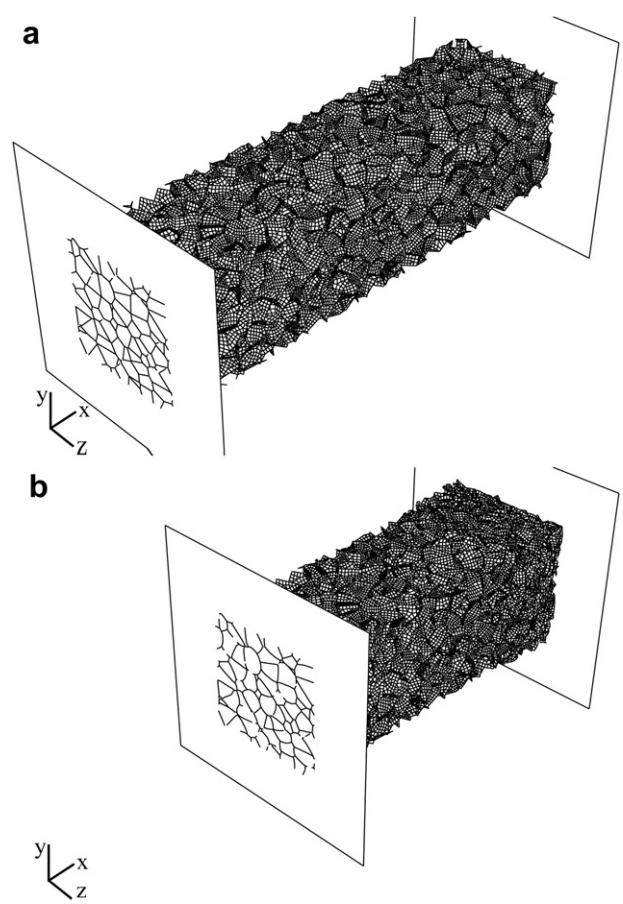

Fig. 8. The rod-target impact of a closed-cell foam: (a) the undeformed configuration and (b) a deformed configuration at $t = 0.4$ ms.

the reflection wave from the fixed end. In real experiments, the deformation process of cellular structures under impact is difficult to observe due to the limit of experimental conditions. Here, the difficulty is solved by using the cell-based simulations. This observation of the deformation process provides important deformation mechanisms of cellular structures, which strongly supports the basis of the shock models.

A comparison of the Lagrangian location of shock front between the cell-based FE model and the shock models is shown in Fig. 6. The Lagrangian location of shock front based on the cell-based FE model is defined as the position near the shock front where the strain declines most rapid. Thus, it can be determined by finding the Lagrangian location along the X axis corresponding to the maximum of the absolute strain gradient within a pre-estimated

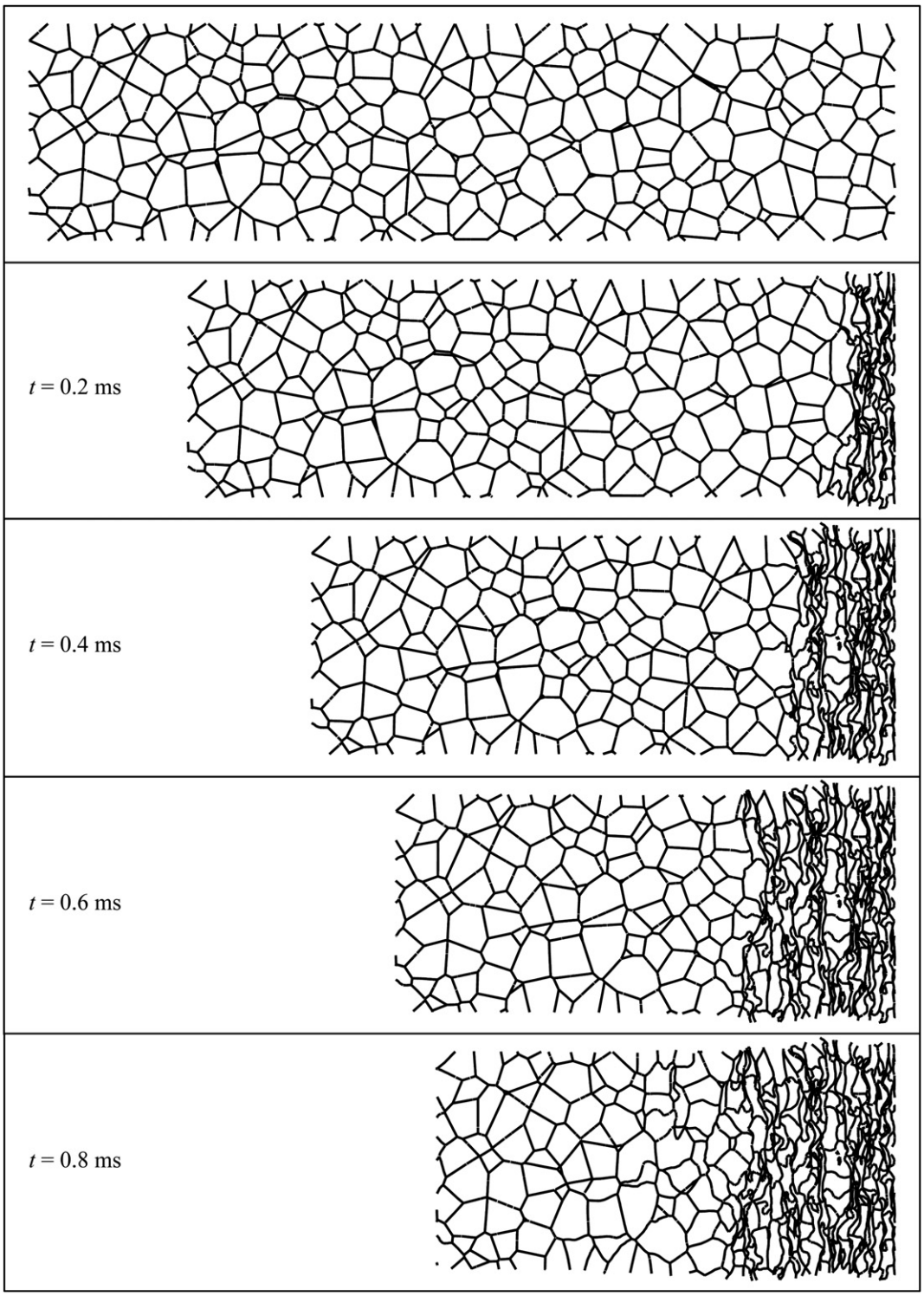

Fig. 9. The undeformed and deformed configurations of the closed-cell foam in the sectional plane of $z = 12.5$ mm, which is a middle plane of the specimen.

interval, in which the strain is very different from that of previous time. For the cell-based model, we only present the results before 4.0 ms because after that time the shock front is not easy to determine. These results compare well with those by the shock models (see Eq. (46)). Hence, the shock models provide well understanding of the high-velocity deformation mechanism of cellular structures. The low-velocity deformation mechanism of irregular honeycomb is through the emergence of random deformation bands. This deformation mechanism of cellular structures is different from that of the shock models, but the shock models still give well prediction of force responses, as shown in Section 4.1.1. It means that the force responses are not sensitive to the location of the deformation band when the impact velocity is low.

4.2. Case 2: A rod-target impact of a closed-cell foam

The choice of the types of the cellular structures and the impact scenario does not affect our main conclusions. As a change, here we focus on the rod-target impact scenario of a much real cellular structure, namely a closed-cell foam.

4.2.1. Force responses

For the rod-target impact scenario, the force responses predicted by the shock models are given by

$$F_{\text{left}} = -M_b a_b = \frac{mA_0\sigma_A(t)}{m+\rho_0\Phi(t)} \tag{87}$$

and

$$F_{\text{right}} = A_0\sigma_B(t). \tag{88}$$

The inertia law is also used to determine the force at the left end of the specimen. These predictions based on three idealisations together with the simulation results of the cell-based model are compared in Fig. 7. The strength enhancement is found at the right end of the specimen, which reduces as the impact time increases. The theoretical predictions are also in good agreement with the numerical FE results.

4.2.2. Deformation features

The deformed configuration of the closed-cell foam at $t = 0.4$ ms is shown in Fig. 8b. As a comparison, the undeformed configuration is presented in Fig. 8a. This comparison shows that the deformation localisation emerges at the right end of the specimen. To get a much impressive understanding, we only consider the configuration in the plane of $z = 12.5$ mm, which is a middle plane of the specimen. The undeformed and deformed configurations in this plane are shown in Fig. 9. Cells collapse layer-by-layer from the right end of the specimen. The cell walls closely parallel to the impact direction deform almost in a buckling manner, while those approximately perpendicular to the impact direction deform likely in a bending manner. A shock front can be detected and the crushing cells locate at this front. The cells far from the front and close to the left end of the specimen almost have no deformation.

The local strain fields have also been calculated using the technique introduced in Appendix C. With the average processing in the Y–Z plane, the strain distribution along the X-direction is determined, where the coordinate system is Lagrangian. The strain distribution when the mass stops ($t_{\text{end}} = 0.890$ ms) is shown in Fig. 10a. For comparison, the strain distributions predicted by the shock models are plotted also in Fig. 10a. In this case, the R-P-P-L model predicts $t_{\text{end}} = 0.86$ ms and the R-PLH model predicts $t_{\text{end}} = 0.98$ ms. It should be noticed that the R-LHP-L model predicts the shock front reaching the left end of the specimen at time

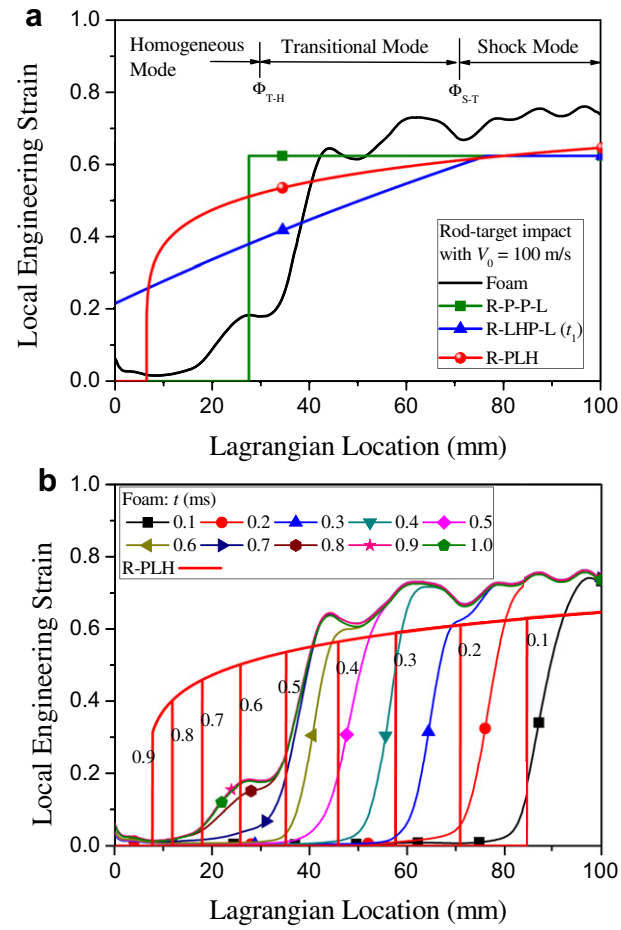

Fig. 10. Local strain distributions along the X-direction of the closed-cell foam: (a) when the striker stops and (b) at different times.

$t_1 = 0.71$ ms. The result of the cell-based model shows that the strain near the left end is very small. Additionally, a comparison of the strain distributions at different times between the cell-based model and the R-PLH model is shown in Fig. 10b. Compared to the cell-based result, the shock models predict slight small strains near the right end of the specimen. This difference may be due to

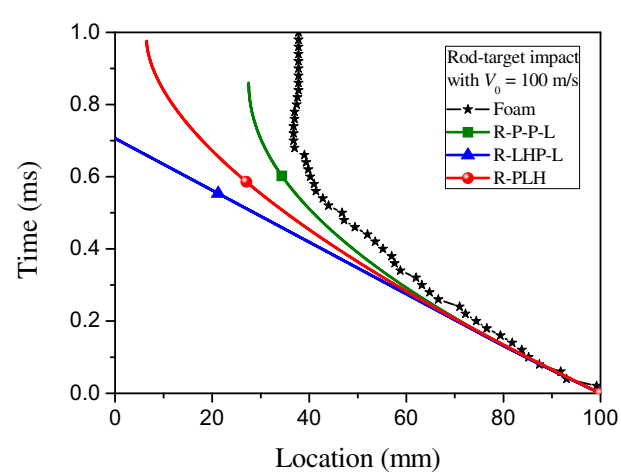

Fig. 11. The impact time versus the Lagrangian location of shock front in the rod-target impact scenario of the closed-cell foam.

some deformation mechanisms such as the micro-inertia effect and the strain-rate effect, which have not been introduced in the present shock models. It may need much evidence and further researches to answer this interesting point. Here, the shock models have well predicted the strength enhancement induced by inertia and presented a first-order understanding of the dynamic crushing behaviour of the closed-cell foam.

A comparison of the Lagrangian location of shock front between the cell-based model and the shock models is shown in Fig. 11. The theoretical predictions (see Eq. (68)) are in good agreement with the numerical FE results when the impact time is short (e.g. $t < 0.3$ ms), and the impact velocity is high enough. With the increase of the impact time, the impact velocity reduces and the shock front moves slowly. Compared to the cell-based results, the shock models overestimate the shock speed when the impact velocity is not high.

5. Conclusions

Different idealisations have been used by many authors in the literature to construct one-dimensional shock models, which can well explain the strength enhancement and the deformation localisation involved in the dynamic responses of cellular materials. A unified framework of one-dimensional plastic shock wave models was presented in this paper. Based on an arbitrary plastic hardening constitutive model for cellular materials, general solutions, although implicit, have been derived for two impact scenarios, namely the striker-rod impact and the rod-target impact, which also can be deduced to two other common impact scenarios, i.e. the plate impact and the Taylor impact. Conservation conditions of mass and momentum across the shock front based on one-dimensional stress wave theory have been used as the basic equations. A combined slope by measuring the average of the slopes of the tangent line and the Rayleigh line and a stress–enhancement parameter characterising the initial stress enhancement were introduced to make the solutions concise.

Based on a power-law hardening constitutive relation of cellular material, closed-form solutions of the physical quantities across the shock front have been derived for the striker-rod impact scenario and semi-closed-form solutions for the rod-target impact scenario. These solutions have taken into account the temporal change of impact velocity. Some transition parameters including the critical impact velocities of modes transitions and several time parameters have been determined. For each impact scenario, the R-PLH model was deduced to two limit cases, i.e. the R-P-P-L model [4] and the R-LHP-L model [10].

The shock models are verified by comparing with cell-based FE simulations. Based on 2D and 3D Voronoi techniques, the striker-rod impact of an irregular honeycomb and the rod-target impact of a closed-cell foam have been considered. Results show that the force responses predicted by the shock models are not very sensitive to the choice of the idealisations and they are in good agreement with the numerical FE results. To characterise the deformation features from the cell-based simulations, the discrete deformation gradient [26,27] was introduced to determine the local strain field. Deformation features predicted by the shock models are compared well with the cell-based results when the impact velocity is high. For low-velocity impact, shock models predict different deformation features, which are also different from the cell-based results. The comparisons show that using more realistic constitutive model such as the R-PLH idealisation may present more accurate predictions. For the closed-cell foam, some other possible deformation mechanisms such as the micro-inertia effect and the strain-rate effect may need to be taken into consideration in further researches.

Acknowledgements

This work is supported by the National Natural Science Foundation of China (Projects Nos. 90916026 and 11002140), the China Postdoctoral Science Foundation (Project No. 20100470860) and the Chinese Academy of Sciences (Grant No. KJCX2-EW-L03).

Appendix A. Nomenclature

A_0	cross-sectional area of the cellular material rod
a_b	acceleration of the rigid mass
C_1	plastic wave speed, $C_1 = (E_1/\rho_0)^{1/2}$
E_0	elastic modulus
E_1	plastic hardening modulus
F	a function $F(q, \zeta)$ defined in Eq. (59)
F^{-1}	the inverse of the function $F(q, \zeta)$
F_{left}	force measured at the left end of specimen
F_{right}	force measured at the right end of specimen
f_1	a function defined in Eq. (19)
f_2	a function defined in Eq. (25)
K	strength index
l_0	length of the cellular material rod
M_b	mass of the striker
m	specific mass defined in Eq. (15)
n	strain-hardening index
q	equivalent strain-hardening index, see Eq. (30)
s	dimensionless variable defined in Eq. (61)
T_1	characteristic time parameter, see Eq. (18)
T_2	characteristic time parameter, see Eq. (24)
t	impact time
t_1	time when the shock front reaches the distal end
t_{end}	time when the striker stops
t_{S-T}	time of mode transition from the shock mode to the transitional mode
t_{T-H}	time of mode transition from the transitional mode to the homogeneous mode
U	internal energy per unit mass
V_0	initial velocity of the striker
V_{c1}	the first critical velocity
V_{c2}	the second critical velocity
v	velocity
v_b	velocity of the striker
x, y, z	Eulerian coordinates
X, Y, Z	Lagrangian coordinates
α	the stress–enhancement parameter, see Eq. (11)
ε	strain
ε_0	initial strain
ε_B	strain behind the shock front
ε_D	densification strain
ε_L	locking strain
ε_{max}	full densification strain
κ	combined slope, see Eq. (13)
μ	ratio of the rod's mass to the striker mass, see Eq. (22)
ρ	local density in the cellular material rod after deformation
ρ_0	initial density of the cellular material rod
σ	stress
σ_0	yield stress of the rod
σ_B	stress behind the shock front
σ_{pl}	plateau stress
τ	dimensionless variable defined in Eq. (81)
Φ	location of the shock front
Q_A	physical parameter ahead of the shock front
Q_B	physical parameter behind the shock front
$\dot{Q}(t)$	a time rate of change of physical parameter Q, i.e. dQ/dt

$Q'(\xi)$ the derivative of physical parameter Q with respect to ξ, i.e. $dQ/d\xi$
$[Q]$ a jump of physical parameter Q across the shock front, see Eq. (4)
$\langle Q \rangle$ mean of physical parameter Q across the shock front, see Eq. (5)
$\{v, \varepsilon, \sigma\}$ a list of important physical parameters

Appendix B. Some mathematical derivations

(a) Derivation of Eq. (16)

Combining Eqs. (12) and (14) leads to a differential equation

$$\frac{\rho_0}{m+\rho_0\Phi}d\Phi = -\frac{\kappa(\varepsilon_B)}{\sigma(\varepsilon_B)}d\varepsilon_B \tag{B.1}$$

Integrating the above equation with the time varying from 0 to t gives

$$\ln\frac{m+\rho_0\Phi(t)}{m+\rho_0\Phi(0)} = -\int_{\varepsilon_B(0)}^{\varepsilon_B(t)}\frac{\kappa(\varepsilon)}{\sigma(\varepsilon)}d\varepsilon. \tag{B.2}$$

With the initial conditions of $\Phi(0)=0$ and $\varepsilon_B(0)=\varepsilon_0$, Eq. (B.2) leads to Eq. (16).

(b) Derivation of Eq. (17)

Substituting Eq. (9) into Eq. (8) with remaining the plus sign, the shock speed is rewritten as

$$\dot{\Phi}(t) = \sqrt{\frac{\sigma(\varepsilon_B(t))-\sigma_0}{\rho_0\varepsilon_B(t)}}. \tag{B.3}$$

By carrying out the differentiation of Eq. (16) with respect to time t, the shock speed can be expressed in another form

$$\dot{\Phi}(t) = -\frac{m}{\rho_0}f_1(\varepsilon_B(t))\dot{\varepsilon}_B(t), \tag{B.4}$$

where f_1 is defined in Eq. (19).

Combining the two forms of the shock speed, i.e. Eqs. (B.3) and (B.4), we obtain

$$dt = -T_1\frac{f_1(\varepsilon_B)\sqrt{\sigma_0\varepsilon_B}}{\sqrt{\alpha\varepsilon_0(\sigma(\varepsilon_B)-\sigma_0)}}d\varepsilon_B. \tag{B.5}$$

Integrating Eq. (B.5) with $\varepsilon_B(0)=\varepsilon_0$ leads to Eq. (17).

(c) Derivation of Eq. (21)

The acceleration of the mass can be determined by two ways: one is by differentiation of the velocity of the mass, i.e.

$$a_b(t) = \frac{dv_b(t)}{dt} = -\frac{\kappa(\varepsilon_B(t))\dot{\varepsilon}_B(t)}{\rho_0\dot{\Phi}(t)} \tag{B.6}$$

with $\kappa(\varepsilon)$ defined in Eq. (13); the other is by the inertia law, i.e.

$$a_b(t) = -\frac{\sigma_0 A_0}{M_b+\rho_0 A_0\Phi(t)} = -\frac{\sigma_0}{m+\rho_0\Phi(t)}. \tag{B.7}$$

Eqs. (B.6) and (B.7) lead to a differential equation

$$\frac{\rho_0}{m+\rho_0\Phi}d\Phi = \frac{\kappa(\varepsilon_B)}{\sigma_0}d\varepsilon_B, \tag{B.8}$$

which can be integrated as

$$\ln\frac{m+\rho_0\Phi(t)}{m+\rho_0\Phi(0)} = \int_{\varepsilon_B(0)}^{\varepsilon_B(t)}\frac{\kappa(\varepsilon)}{\sigma_0}d\varepsilon. \tag{B.9}$$

With the initial conditions $\Phi(0)=l_0$ and $\varepsilon_B(0)=\varepsilon_0$, Eq. (B.9) leads to Eq. (21).

(d) Derivation of Eq. (23)

Substituting Eq. (20) into Eq. (8) with remaining the minus sign, the shock speed can be determined as

$$\dot{\Phi}(t) = -\sqrt{\frac{\sigma(\varepsilon_B(t))-\sigma_0}{\rho_0\varepsilon_B(t)}}. \tag{B.10}$$

The shock speed also can be determined by carrying out the differentiation of Eq. (21) with respect to time t, i.e.

$$\dot{\Phi}(t) = \frac{m}{\rho_0}(1+\mu)f_2(\varepsilon_B(t))\dot{\varepsilon}_B(t), \tag{B.11}$$

where f_2 is defined in Eq. (25). Combining Eqs. (B.10) and (B.11) gives

$$dt = -T_2\frac{f_2(\varepsilon_B)\sqrt{\sigma_0\varepsilon_B}}{\sqrt{\alpha\varepsilon_0(\sigma(\varepsilon_B)-\sigma_0)}}d\varepsilon_B. \tag{B.12}$$

Integrating Eq. (B.12) with the initial condition of $\varepsilon_B(0)=\varepsilon_0$ leads to Eq. (23).

Appendix C. Local strain

The discrete deformation gradient based on the method of least squares [26,27] is employed here to determine the local strain field of cellular structures. The undeformed configuration and a deformed configuration are taken from the cell-based finite element simulation. The coordinates of node i in the undeformed and deformed configurations are denoted as $\mathbf{X}_i$ and $\mathbf{x}_i$, respectively. A set N_i for node i collects any node j that has a distance from node i less than a cutoff distance R_c in the undeformed configuration. Here, the cutoff distance R_c is taken to be 1.5 times of the average cell size of the specimen. For each neighbour j of node i, their distances in the two configurations are given by $\mathbf{D}_{ji}=\mathbf{X}_j-\mathbf{X}_i$ and $\mathbf{d}_{ji}=\mathbf{x}_j-\mathbf{x}_i$. The best mapping of the two configurations gives the deformation gradient tensor

$$\mathbf{F}_i = \mathbf{V}_i^{-1}\mathbf{W}_i, \tag{C.1}$$

where $\mathbf{V}_i = \sum_{j\in N_i}\mathbf{D}_{ji}^T\mathbf{D}_{ji}$ and $\mathbf{W}_i = \sum_{j\in N_i}\mathbf{D}_{ji}^T\mathbf{d}_{ji}$. The Lagrangian strain tensor for node i can be then calculated as

$$\mathbf{E}_i = \frac{1}{2}(\mathbf{F}_i\mathbf{F}_i^T-\mathbf{I}). \tag{C.2}$$

The local strain field is achieved using tessellation-based linear interpolation. The desired strain in this paper is the local engineering strain in the X-direction, which is determined as

$$\varepsilon_1 = 1-\sqrt{1+2E_{11}}, \tag{C.3}$$

taken as positive in compression.

References

[1] Reid SR, Peng C. Dynamic uniaxial crushing of wood. Int J Impact Eng 1997; 19(5–6):531–70.
[2] Harrigan JJ, Reid SR, Peng C. Inertia effects in impact energy absorbing materials and structures. Int J Impact Eng 1999;22(9–10):955–79.
[3] Tan PJ, Reid SR, Harrigan JJ, Zou Z, Li S. Dynamic compressive strength properties of aluminium foams. Part I—experimental data and observations. J Mech Phys Solids 2005;53(10):2174–205.
[4] Tan PJ, Reid SR, Harrigan JJ, Zou Z, Li S. Dynamic compressive strength properties of aluminium foams. Part II—'shock' theory and comparison with experimental data and numerical models. J Mech Phys Solids 2005;53(10):2206–30.
[5] Hanssena AG, Enstockb L, Langsetha M. Close-range blast loading of aluminium foam panels. Int J Impact Eng 2001;27:593–618.
[6] Main JA, Gazonas GA. Uniaxial crushing of sandwich plates under air blast: Influence of mass distribution. Int J Solids Struct 2008;45:2297–321.
[7] Radford DD, Deshpande VS, Fleck NA. The use of metal foam projectiles to simulate shock loading on a structure. Int J Impact Eng 2005;31(9):1152–71.
[8] Zheng ZJ, Yu JL, Li JR. Dynamic crushing of 2D cellular structures: a finite element study. Int J Impact Eng 2005;32(1–4):650–64.
[9] Yu JL, Liu YD, Zheng ZJ, Li JR, Yu TX. Influences of inertia and material property on the dynamic behavior of cellular metals. In: Zhao H, Fleck NA, editors. Iutam symposium on mechanical properties of cellular materials. Dordrecht: Springer; 2007. p. 149–57.
[10] Zheng ZJ, Liu YD, Yu JL, Reid SR. Dynamic crushing of cellular materials: continuum-based wave models for the transitional and shock modes. Int J Impact Eng 2012;42:66–79.
[11] Lopatnikov SL, Gama BA, Haque MJ, Krauthauser C, Guden M, Hall IW, et al. Dynamics of metal foam deformation during taylor cylinder–hopkinson bar impact experiment. Compos Struct 2003;61(1–2):61–71.
[12] Lopatnikov SL, Gama BA, Haque MJ, Krauthauser C, Gillespie Jr JW. High-velocity plate impact of metal foams. Int J Impact Eng 2004;30(4):421–45.
[13] Lopatnikov SL, Gama BA, Gillespie Jr JW. Modeling the progressive collapse behavior of metal foams. Int J Impact Eng 2007;34(3):587–95.
[14] Li QM, Reid SR. About one-dimensional shock propagation in a cellular material. Int J Impact Eng 2006;32(11):1898–906.
[15] Elnasri I, Pattofatto S, Zhao H, Tsitsiris H, Hild F, Girard Y. Shock enhancement of cellular structures under impact loading: part I experiments. J Mech Phys Solids 2007;55(12):2652–71.
[16] Pattofatto S, Elnasri I, Zhao H, Tsitsiris H, Hild F, Girard Y. Shock enhancement of cellular structures under impact loading: part II analysis. J Mech Phys Solids 2007;55(12):2671–86.
[17] Zou Z, Reid SR, Tan PJ, Li S, Harrigan JJ. Dynamic crushing of honeycombs and features of shock fronts. Int J Impact Eng 2009;36(1):165–76.
[18] Harrigan JJ, Reid SR, Tan PJ, Reddy TY. High rate crushing of wood along the grain. Int J Mech Sci 2005;47(4–5):521–44.
[19] Harrigan JJ, Reid SR, Yaghoubi AS. The correct analysis of shocks in a cellular material. Int J Impact Eng 2010;37(8):918–27.
[20] Wang LL. Foundations of stress waves. Amsterdam: Elsevier Science Ltd; 2007. p. 35–42.
[21] Liu YD, Yu JL, Zheng ZJ, Li JR. A numerical study on the rate sensitivity of cellular metals. Int J Solids Struct 2009;46(22–23):3988–98.
[22] Yu JL, Zheng ZJ. Dynamic crushing of 2D cellular metals: microstructure effects and rate-sensitivity mechanisms. Acta Mech Solida Sin 2010;23(S):45–55.
[23] Wang CF, Zheng ZJ, Yu JL. Micro-inertia effect and dynamic Poisson's ratio of closed-cell metallic foams under compression. In: Fan JH, Zhang JQ, Chen HB, Jin ZH, editors. Advances in heterogeneous material mechanics. Lancaster: DEStech Publications; 2011. p. 266–9.
[24] Miltz J, Ramon O. Energy absorption characteristics of polymeric foams used as cushioning materials. Polym Eng Sci 1990;30(2):129–33.
[25] Avalle M, Belingardi G, Montanini R. Characterisation of polymeric structural foams under compressive impact loading by means of energy-absorption diagram. Int J Impact Eng 2001;25:455–72.
[26] Li J, Shimizu F. Least-square atomic strain. Report in June 12, http://mt.seas.upenn.edu/Archive/Graphics/A/annotate_atomic_strain/Doc/main.pdf; 2005.
[27] Gullett PM, Horstemeyer MF, Baskes MI, Fang H. A deformation gradient tensor and strain tensors for atomistic simulations. Model Simul Mater Sci Eng 2008;16:015001.